ORIGINAL ARTICLE

Comprehensive approach to in silico identification and in vitro validation of anti-filarial hit molecules targeting the dimer interface of thioredoxin peroxidase 1 in *Wuchereria bancrofti*: a progress in anti-filariasis drug development

Muthusamy Sureshan[1] · Sundarraj Rajamanikandan[2] · Kadhirvel Saraboji[3]

Abstract

Lymphatic filariasis (LF) remains a significant health challenge for populations in developing countries. LF is a parasitic disease transmitted by mosquitoes, mainly caused by the filarial nematode, *Wuchereria bancrofti*, prevalent in tropical and subtropical regions. Since the present drugs develop complications, including adverse side effects, lack of specificity, and development of drug resistance, the present study focused on developing the potential anti-filariasis drugs targeting crucial proteins for the nematode life cycle. We have identified the therapeutic compounds by targeting the enzyme thioredoxin peroxidase 1 (*Wb*TPx1), which facilitates the conversion of hydrogen peroxide into water, an essential mechanism by which the nematode survives against oxidative stress in the host. This approach might resolve treatment efficacy and activity difficulties at various stages of filarial parasitic worms. We modeled the structure of *Wb*TPx1 and employed the structure-based virtual screening approach, focusing on the dimer interface region of the protein. ADMET prediction profiles of the non-toxic, top-ranked hits with higher docking scores demonstrate higher affinity to the nematode protein than its human homolog. The molecular dynamic simulation studies show *Wb*TPx1-hit complexes' stability and the intactness of hits in the binding site. Further, in vitro validation of identified hits using *Setaria digitata*, a cattle nematode, showed better IC_{50} and higher inhibition than the standard drug ivermectin, indicating the potential to inhibit enzyme activity and the development of drug candidates for controlling LF.

Keywords *Wuchereria bancrofti* · *Wb*TPx1 · Molecular docking · MTT

Introduction

Lymphatic filariasis (LF), is a disease transmitted to humans by infected mosquitoes. It is also known as elephantiasis, and this disfiguring disease is caused by three different species of parasitic nematodes: *Brugia malayi, Brugia timori,* and *Wuchereria bancrofti* and more than 90% of cases were reported by *W. bancrofti* [1, 2]. Early report states that, the number of people affected due to LF stands at around 120 million across 76 countries throughout the tropical regions of Africa, Asia, and other sub-tropical regions [3, 4]. Another insight is that India and Sub-Saharan parts of Africa are the major regions affected by LF. As per the 2021 World Health Organization (WHO) statistics, LF continues to concern 882 million people in 44 countries worldwide. According to the global baseline estimate, over 15 million people were affected by lymphedema and 25 million males from hydrocele. If we consider the filarial infection in Asia, it accounts for nearly 63% global burden, mostly in the region of Southeast Asia, India alone harbors 40% of the world filarial burden, despite the existence of the National Filaria Control Programme (NFCP) since 1955 [5]. This vector-borne disease is transmitted to humans,

✉ Kadhirvel Saraboji
sarabojik@gmail.com; saraboji.kadhirvel@cup.edu.in

1 Biomolecular Crystallography Lab, Department of Bioinformatics, School of Chemical & Biotechnology, SASTRA Deemed University, Thanjavur 613401, India

2 Department of Biochemistry, Centre for Drug Discovery, Karpagam Academy of Higher Education, Coimbatore 641021, India

3 Department of Computational Sciences, Central University of Punjab, Bathinda, Punjab 151401, India

especially through the members of the *Aedes, Anopheles, Culex, Mansonia,* and *Ochlerotatus* mosquitoes that serve as carriers, transmitting them based on the unique biological characteristics and geographic locations [6]. Eventually, they grow and affect the lymphatic system, causing permanent damage to humans and leading to disfiguration and disability of the limbs. Being a digenetic parasite, *W. bancrofti* has its lifecycle in two hosts. The humans support the adult form, and the mosquitoes support the larval form. During a blood meal, the mosquito injects infectious filarial larvae into a healthy human, where they developed in the lymphatic system into adult worms. Over a period, these adult undergo sexual reproduction giving rise to larval offspring referred to as microfilariae. Subsequently, these microfilariae migrate from lymphatic system into bloodstream and perpetuating the cycle when mosquito ingest the blood from infected person [7, 8]. WHO formed GPELF (Global Programme to Eliminate Lymphatic Filariasis) in 1997, where Mass Drug Administration (MDA) and morbidity management activities were initiated to educate people on personal hygiene management and the health impact of preventing LF. Ivermectin, albendazole (ALB), and diethylcarbamazine (DEC) are generally used to treat filarial worms. However, their mechanism has yet to be deciphered clearly, and these drugs works well for larval stage of the worms and not against adult and larval parasites [9, 10]. Currently the filarial treatment switching from two-drug regimen to a three-drug regimen with the combination of ivermectin, diethylcarbamazine, and albendazole (IDA) in addition, chemotherapy was also given as medication. The major problem in the current treatment for LF is that the exact mechanism of the anti-filarial are not known clearly and development of drug resistance to its molecular targets. Due to the prolonged use of these drugs, the nematode developed resistance due to the single nucleotide polymorphisms in its molecular targets. These drugs have developed resistance due to SNPs, mutations and lack of specificity with the filarial targets. Ivermectin exhibit varying therapeutic efficacy due to the polymorphisms in cytokine genes IL-10, TGF-β, IFN-γ, IL-4 and IL-5 that hinder the success rate of the treatment of LF [11]. Because of the existing mutations in the gene that encodes β-tubulin in the filarial worm, drug resistance has been developed in albendazole. It was reported that DEC alters the host arachidonic acid and nitric oxide metabolic pathways and it showed extreme adverse side effects and is not recommended for treating LF [12]. Mutations that confer resistance to anthelmintic medications can emerge on their own or become more prevalent as a result of pharmacological therapy. There is no conclusive evidence establishing a clear relationship between these genes and the development of resistance [13].

Upon *W. bancrofti* infection, the host's initial immune system reaction activates macrophages, neutrophils, and eosinophils. This response hits to the production of ROI "Reactive Oxygen Intermediates" and RNI "Reactive Nitrogen Intermediates", which include the superoxide anion radical (O_2^-), hydrogen peroxide (H_2O_2), peroxyl (RO_2·) and hydroxyl radicals (OH^-). Collectively, referred to as ROS (reactive oxygen species) generated by the host to manage the nematode invasion [14, 15]. Nevertheless, the primary characteristics of a lymphatic filariasis infection involve the nematode's ability to survive within the host for an extended period (years). Their effective neutralization of ROS facilitates this resilience through well-adapted antioxidant enzymes. The crucial survival tactic employed by filarial nematodes revolves around their antioxidant enzymes, which include catalase (CAT), glutathione peroxidase (GPx), glutathione S transferases (GST), peroxiredoxins (Prxs) and superoxide dismutase (SOD). These enzymes are essential in neutralizing the ROS activity of the host, thereby securing the ongoing viability of the nematodes within the host [16, 17]. So, focusing on these antioxidant enzymes might serve as a viable and effective approach to target the worms at all phases of their life cycle. Peroxiredoxins (Prxs) display remarkable efficiency as cysteine-dependent peroxidases actively participating in antioxidant, regulatory, and signaling systems with remarkable efficiency. Prxs play a crucial role in defending against peroxynitrite ($ONOO^-$) and ROS that arise from both the host and endogenous sources [18]. A widespread family of peroxidases found in most of the eukaryotes, Prxs play a critical role in reducing hydrogen peroxide (H_2O_2), peroxynitrite, and alkyl hydroperoxides of various affinities. The active site, catalytic cycle, and fold of prxs were conserved and they interact with the peroxide substrate through a conserved cysteine residue known as the peroxidatic Cys (CP) [19, 20]. Peroxiredoxins may be categorized into five subfamilies: BCP, Prx1, Prx5, Prx6 and Tpx based on sequence similarity. Thioredoxin peroxidase-1 (TPx-1) is a member of the thiol-specific antioxidant protein family that is mostly found in the cytoplasm and they effectively reduced and detoxified the H_2O_2 using the redox-active cysteine. Three varieties of TPxs are distinguished by the location and number of cysteine (Cys) residues: 1-Cys, typical 2-Cys, and atypical 2-Cys type [21, 22]. They follow a uniform reaction mechanism in which the catalytic cysteine, referred to as the peroxidatic cysteine, undergoes oxidation by hydroperoxides, resulting in hyper oxidation and forming sulfenic (–SOH), sulfinic (–SO$_2$H), or sulfonic acid (–SO$_3$H) states of the cysteine. Subsequently, the cysteine is regenerated to its reduced form by various molecules, such as thioredoxin (TRX), glutaredoxin (GRX) or glutathione [23]. Because the filarial parasite is susceptible to disruption of its antioxidant system, it is an ideal potential target for developing new drug candidates [24].

In the present work, we used the in silico methods to modeled and study the dynamic structural stability of *Wb*TPx1 using homology modeling and simulation studies. To identify promising hits that could bind with *Wb*TPx1 we performed structure-based virtual screening. Moreover, the potent hit molecules undergo complex dynamics using molecular dynamics (MD) simulations to evaluate their dynamic intactness with the enzymes. The quantum mechanical method DFT (Density Functional Theory) examines the reactivity of identified hits. The hit compounds identified in the present study were further substantiated through in vitro validation using *Setaria digitata*. Our study's findings and associated observations could pave the way for designing and developing innovative therapeutic drug compounds that could effectively target the filarial worm throughout its whole life cycle, with the ultimate goal of eradicating LF.

Materials and methods

Modeling of thioredoxin peroxidase 1 (TPx1) of *Wuchereria bancrofti* (*Wb*TPx1)

Homology modeling techniques have been employed to predict a reliable 3D structure as target protein since experimental 3D structure of *Wb*TPx1 is not been reported. The *Wb*TPx1 (UniProt ID: B8YNX5) has a 228 amino acid protein sequence that was obtained from the UniProt sequence database. To find the best template, BLASTp was utilized to search against the Protein Databank (PDB) and the determination of the optimal template relied on factors such as E-value, query coverage, percentage identity, and resolution. The Schrödinger Prime suite [25] was used to model the 3D coordinates of *Wb*TPx1 using the best template structure and the structural deviation was calculated for the selected template and target using PyMol. The PROCHECK module present in SAVES server was used to examine the stereochemistry for the modeled structure.

Molecular dynamics simulations of *Wb*TPx1

The GROMACS 5.1.2 suite [26] was utilized to carried out MD simulation to study the dynamicity of *Wb*TPx1 using GROMOS96 53a6 force field [27] to create the protein topology. The *Wb*TPx1 system was parameterized with a 1.2 nm dimension in every direction at the center of the cubic box. Using an SPC water model, the system was solvated with about 22,958 water molecules [28]. The system's total charge was neutralized by introducing the proper quantity of 0.1 M ionic strength sodium (Na^+) and chloride (Cl^-) ions. To eliminate the steric conflicts and poor geometry in the solvated system, the energy minimization was implemented using steepest descent method [29] for maximum of 50,000 steps, then the system was brought to equilibrium for 500 ps under the NVT ensemble (isothermal-isochoric) with constant particles, volume and temperature using the Berendsen external bath [30]. Further, Parrinello-Rahman barostat [31] was used to equilibrate for 2000 ps with constant particles, pressure and temperature under NPT ensemble (isothermal-isobaric) at 310 K. LINCS algorithms [32] were implement to constraint the bond and bond length and the geometry of the solvent were constraints by implementing the SETTLE algorithm [33]. Applying the Particle Mesh Ewald (PME) method, the long-range electrostatic interactions were computed [34]. Finally, production MD simulation was applied to the well-equilibrated protein system for 200 ns time scale, storing structure trajectories every 10 ps. The dynamic stability profile of the *Wb*TPx1was examined by analyzing the fluctuations in the RMSF, RMSD, Rg and SASA by GROMACS utilities and VMD [35] was used to analyze and visualize the trajectories.

Preparing the *Wb*TPx1 for structure-guided virtual screening

The Schrödinger suites VSW (Virtual Screening Workflow) module was utilized to screen for potential inhibitors. Ligand Preparation, Filtering, and Docking are the three main process in VSW. First, the Ligprep module was used to prepare the small molecules dataset [36], which involves the conversion of 2D into 3D conforms using the OPLS-3e force field [37] that generates up to 32 conformations for each molecule. The ligand molecules prepared were allowed to pass through the filters based on the "Lipinski rule of five", ADME properties, and the elimination of compounds with special reactive groups, such as alkali metals and halogens. Next, we prepared the *Wb*TPx1 protein using Schrödinger protein preparation wizard, which refines and corrects the charges, bond order, bond angle, and side chains of the atoms in proteins. By utilizing the OPLS-3e force field, the intra-molecular hydrogen bonds were optimized, and the modeled structure underwent energy minimization. Identifying and selecting suitable binding pockets have become an essential aspect of computational screening. By utilizing the Schrödinger SiteMap module [38], we predict the binding site of the *Wb*TPx1. It calculates the properties of the residue includes acceptor, donor, and hydrophilic regions in *Wb*TPx1 and ranks the possible binding pocket based on the SiteScore function. Finally, the best-ranked binding site was chosen for docking, the grid box was created with 15 Å from all three sides that cover all the residues. Glide module of Schrödinger [39], uses the three-stage docking method to identify the best binding small molecules which covers HTVS (High Throughput Virtual Screening),

SP (Standard Precision) and XP (Extra Precision). In each docking stage, only top 10% of the molecules were allowed for the subsequent level of virtual screening. Further, Prime MM-GBSA modules which use the OPLS-AA force field to perform the ΔG_{bind} (binding free energies) calculation for the WbTPx1-ligand bound complexes with default parameters.

Density functional theory (DFT) studies

Top five identified hits compounds were taken for the DFT calculation using the Gaussian 09 program [40]. The electronic structure is a fundamental component in understanding the thermodynamic properties of molecular interactions and the electronic, chemical, and molecular dynamics nature of small molecules. To identify the energy levels of the "Highest Occupied Molecular Orbital" (HOMO) and "Lowest Unoccupied Molecular Orbital" (LUMO) for the identified hits using the hybrid function B3LYP-D3 with the basis set 6-311G**++(2d, 2p). Calculating the energy gap (HOMO–LUMO) enables the determination of various electronic properties, including chemical potential, chemical stability, electron affinity and hardness [41]. This information is critical in comprehensively assessing the chemical potential of the hits and helps in understanding their electronic properties.

Stability analysis of protein–ligand complexes

The MD simulations assess the dynamic stability of the best five non-toxic hits complex with the WbTPx1. The hit topologies were parameterized using the online PRODRG server [42]. The WbTPx1-hit complexes system was constructed similarly implemented in native WbTPx1, which includes replicating the protein topology, setting up the system using the periodic boundary condition, solvation, neutralization and equilibration. The dynamicity of the complexes was investigated by performing 50 ns production MD simulation.

Essential dynamics (PCA) for the native and hits bound WbTPx1

To analyze the conformational changes and atomic movements of WbTPx1 and hit-bound WbTPx1 complexes, the PCA (Principal Component Analysis) was employed to the their respective trajectory structure obtained from MD simulations [43]. PCA is a popular statistical technique used to investigate the protein movements that are crucial to understanding the biological roles [44]. The unsupervised multivariate statistical method that explains the greatest variability across the datasets is often used to reduce the dimensionality of large datasets [45]. The initial step in

PCA construction is to prepare the trajectory in cartesian coordinates, that involves eliminating the solvents and periodicity that establish the necessary initial parameters, then the next crucial metrics is the construction of a covariance matrix with dimensions of $3N \times 3N$, where N represent the overall number of atoms in trajectory obtained from simulation studies for the WbTPx1 and hit-bound systems. The eigenvectors and eigenvalues that describe the motion and magnitude of the WbTPx1 are obtained through the diagonalization of the covariance matrix [46]. Most often, the highest variability in the data can be attributed to the first three eigenvalues, which correspond to the principal components PC1, PC2, and PC3. Using the bio3D package in R software, the PCA analysis was carried out on the WbTPx1 protein in two distinct states: the unbound-native and hit-bound WbTPx1 [47].

Anti-filarial activity using in vitro studies

Setaria digitata, a filarial worm that infects cattle and is homologous to human parasites *W. bancrofti*, was used in in vitro tests to evaluate the hit compounds identified through in silico approaches [48, 49]. *S. digitata* is a well-known and extensively studied in vitro model organism popularly used for testing the macrofilaricidal activity [50–52]. Adult motile worms are collected from the peritoneal cavity of a calf that had been newly slaughtered, and they were subsequently washed multiple times using normal physiological saline (0.95%). Without delay, the adult worms were expeditiously transferred into DMEM (Dulbecco's modified eagle's medium), with 0.01% Pen-Strep antibiotic and 10% heat-inactivated fetal bovine serum (FBS) and the container was brought to the lab less than an hour. The chemical compounds were acquired from San Diego, California's ChemBridge Corporation. To evaluate the viability of *S. digitata*, the MTT (3-(4,5-dimethylthiazol-2-yl)-2,5-diphenyltetrazolium bromide) reduction assay was performed. The worms were exposed to different concentrations (0.625, 1.250, 2.500, 5.000, 10.000, 15.000, and 20.000 μM), for a duration of 24 h [53]. Pen-Strep (0.01%) and 10% heat-inactivated FBS were added to DMEM throughout testing [54]. Each worm was exposed for 24 h before being incubated for 30 min with.

0.25 mg mL^{-1} MTT on phosphate-buffered saline (pH 7.4). After the incubation period was over, each worms were moved into microplate plate with 400 μL dimethyl sulphoxide (DMSO) and allowed to gently shake for an hour at room temperature. Using a multimode plate reader (Synergy H1, BioTek, USA), the absorbance of formazan produced by treated–T, control–C (untreated), and negative control –H (heat-killed worms) was measured at 492 nm.

$$Percentage\ of\ inhibition = 100 - \left[\frac{(T-H)}{(C-H)}\right] \times 100$$

The positive control group consisted of adult worms that were exposed to media but not treated with hits. The negative control (H) were heat-killed adult worms for 30 min at 56 °C and then incubated with MTT. The concentration of the inhibitor and the percentage of inhibition from the triplicate tests and controls were used to generate the inhibition profile [54, 55]. Using GraphPad PRISM 8.0.1, the IC$_{50}$ values using dose–response are determined and matched with reference drug, ivermectin.

Results and discussion

Modeling and validation of *Wb*TPx1

The sequence similarity search was carried out against non-redundant RCSB-PDB using NCBI-BLASTp that identified the crystallographic structure of peroxiredoxin-1 (PDB ID: 4FH8) from *Ancylostoma ceylanicum* (AcePrx-1) as the best template with the sequence identity of 64.71% along with the query coverage of 82% and e-value of 1e-^{89}. Thus, the 3D structure of *Wb*TPx1 was modeled using the template (PDB ID: 4FH8) and the structural alignment showed an RMSD deviation of 0.68 Å. The quality of the modeled *Wb*TPx1 3D structure (Fig. 1) is demonstrated by the Ramachandran plot with respect to φ and ψ angles, which shows that 75.3%

of amino acid residues are present in the most favored regions, 22.2% are in additional allowed region, 2.5% are in the generously allowed region, and none (0.0%) of the amino acids were observed in the disallowed regions, the detail statistics of the Ramachandran plot is given in Supplementary Fig. 1. The *Wb*TPx1 possesses an amino acid of 228 residues that forms a compact and globular structure featuring the characteristic fold of the Prxs (peroxiredoxins) family that is organized around a twisted sheet composed of seven β-strands, encircled by five α-helices, particularly it forms thioredoxin fold-a unique structural motif consists of four-stranded β-sheet and three flanking α-helices [56]. The existence of conserved motif ''GGLG'' (Gly-Gly-Leu-Gly) and ''YF'' (Tyr-Phe) that are the invariant features of Prxs family, the sequence of *Wb*TPx1 also found to have conserved motif as like in other parasites [18]. The amino acid sequence of *Wb*TPx1 has two peroxidative cysteine residues (conserved cysteine) at positions 78 and 199 that are essential for the reduction and detoxification of hydrogen peroxides as well as aiding in head-to-tail dimer interface formation composed of residues 166 to 192 as remain conserved across Prxs family [19].

Dynamic stability studies of *Wb*TPx1 through MD simulations

The MD simulation were performed for 200 ns at 310 K in the SPC water model to examine the dynamicity of *Wb*TPx1. The processed trajectories (20,000 structures) were used
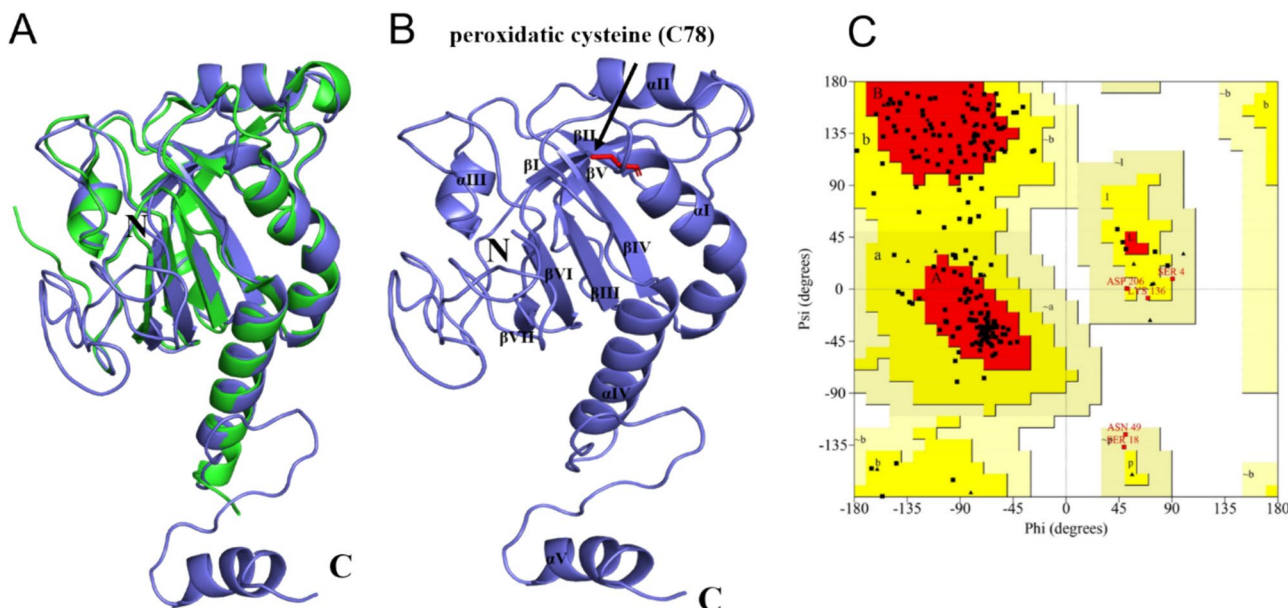
Fig. 1 A Superimposition between target (*Wb*TPx1) and the template (*Ancylostoma ceylanicum,* Peroxiredoxin-1 **B** Cartoon illustration of a three-dimensional structure of *Wb*TPx1 that characterized with thioredoxin fold consisting of five α-helices and seven β-strands and the catalytic important residues peroxidatic cysteine (C78) are represented as red sticks, and **C** Ramachandran Plot for the *Wb*TPx1 model

to study the dynamic structural changes in the *Wb*TPx1. After 20 ns, it was observed that the systems had achieved a stable equilibrium. The RMSD of *Wb*TPx1 was plotted, which showed a deviation between 0.38 and 0.49 nm with the average RMSD and standard deviation of 0.44 nm and 0.015 nm, respectively. A lower deviation in the RMSD value signifies dynamic stability and equilibrium in the modeled structure, making it suitable for further studies. The RMSF was calculated to assess and evaluate the each amino acid residue flexibility of in *Wb*TPx1, the residue-specific flexibility along the backbone of the *Wb*TPx1 exhibits RMSF between 0.04 and 0.51 nm with average RMSF and SD of 0.15 nm and 0.09 nm, respectively.

It was noted that the region of the N-terminal loop of *Wb*TPx1, starting from Met1 to Phe42, showed higher fluctuations. In contrast, the residue Ser23 exhibited the highest N-terminal fluctuation with the RMSF value of

0.46 nm. The loop-III which spans from Met57 to Lys63, which connects the β-sheet III (β-III) with the α-helix I (α-I), exhibits a higher backbone fluctuation between 0.08 nm (Met57) and 0.12 nm (Lys61). The longer loop-V that starts from Thr116 to Pro129 showed fluctuation between 0.05 (Pro129) and 0.17 nm (Glu120). Similarly, the loop-VI (143–154 residues) that connect the α-III with β-V showed higher residual fluctuation that ranged from 0.10 to 0.23 nm; among them, the residue Glu148 had the maximum fluctuation. Additionally, the C-terminal region, ranging from residues 195 to 228 and encompassing loop-IX and α-V, exhibited higher fluctuations, mainly because of its inherent flexibility in terminal.

The RMSF analysis revealed that the elevated fluctuations noted in the amino acid residues align in the loops of C- and N-terminals of the *Wb*TPx1. The dynamic compactness of the *Wb*TPx1 was monitored based on changes in the Rg, that
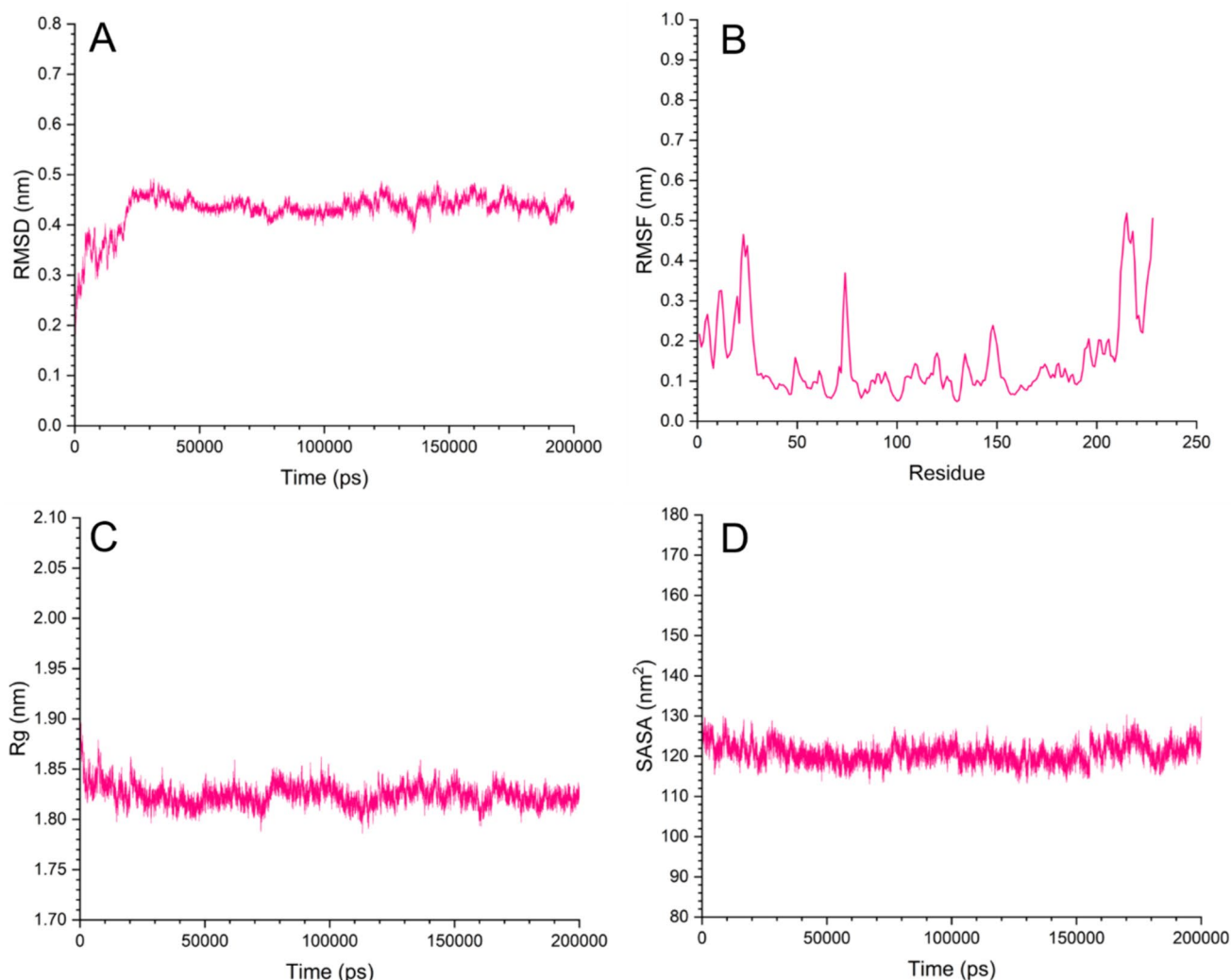
Fig. 2 The data indicate that the *Wb*TPx1 is stable and preserves its structural architecture throughout the simulation: (**A**) RMSD, (**B**) RMSF, (**C**) Rg and (**D**) SASA calculated from 200 ns simulations

fluctuate between 1.78 nm and 1.89 nm, averaging 1.82 nm. This observation indicates the structural compactness and stability of the intact architecture of *Wb*TPx1 during the simulation. Further, the SASA was computed to evaluate the folding profile and the protein's interaction to solvent molecules over time, the SASA value for *Wb*TPx1 was found between 113 and 130 nm^2, with an average of 120 nm^2 (Fig. 2). These overall MD simulation results revealed that the modeled *Wb*TPx1 is stable with intact structural architecture during the timescale of 200 ns MD simulation.

Prediction of binding site and structure-guided virtual screening of *Wb*TPx1 inhibitors

The Schrödinger SiteMap module, we identify the regions of the binding sites in *Wb*TPx1, we utilized the potentially energy minimized structure (− 968439.19 kJ/mol) obtained from the 200 ns trajectories structure for binding site predictions and molecular docking studies, the detailed of all the predicted sites of *Wb*TPx1 are shown in supplementary Fig. 2 and the best site is selected based on the site score, Dscore (druggability score) and volume. The predicted site revealed a highest site score of 0.929 and a druggability score of 0.957 with the cavity volume of 315.217 Å^3 through diverse descriptors such as enclosure, size, cavity, volume, solvent exposure degree, interaction tightness, and hydrogen bond donor and acceptor characteristics. The predicted binding site comprises the following residues: Ser8, Leu27, Ala28, Ile30, Pro35, Ile165, Arg166, His167, Ser168, Leu169, Val170, Glu181, Arg184, Thr185, Ala188, Phe189, Val192, Glu193, Glu197, Val198, Cys199, Pro200, Ala201, Asn202 and Trp203, respectively. Interestingly, the predicted binding site lies in the reported region involved in the dimer interface (166 to 192) [57], and targeting the interface region was reported to be a successful approach in inhibiting the activity of proteins and enzymes [58–60]. The grid for docking was created to cover all the binding site residues of *Wb*TPx1 using the grid size of $X = 53.05$, $Y = 47.62$, and $Z = 47.15$ with the inner grid box of $10 \times 10 \times 10$ Å^3 and the outer grid dimensions of $32.41 \times 32.41 \times 32.41$ Å^3 to perform molecular docking within the specified grid space boundaries. To screen against *Wb*TPx1, we used small molecule compounds from the in-house ChemBridge database, the prefiltering first eliminates molecules with reactive functional groups and those that violate the five rules of Lipinski. Approximately 698,709 small compounds from the ChemBridge database were chosen following the filtering procedure. The final dataset, which consisted of 2,086,614 structures, was carefully prepared and then subjected to a three-phase molecular docking steps (HTVS, SP, and XP) for screening against *Wb*TPx1, finally a total of 601 molecules in with docking scores ranging from − 7.84 to − 5.46 kcal/mol were obtained based on XP results

following screening using HTVS and SP docking. The top 25 hit compounds (Supplementary Table 1) were tested for toxicity profile prediction using the Mclue server, based on their binding affinity for *Wb*TPx1 [61].

The prediction revealed five non-toxic hit molecules (ChemBridge ID: 26319496, 58522350, 24425757, 38651207 & 29025530) and ADME calculations indicate that the molecules are in the acceptable range (Table 1). The highest drug-likeliness attribute is represented by the #star descriptor value of zero across the top five non-toxic hits, signifying a higher probability of drug-like quality. All the top five hits exhibit favorable aqueous solubility, cell permeability, absorption, and zero violation in Lipinski's rule of five, which clearly depict the identified hits have higher oral bio-availability. The extra Precision (XP) docking results (Fig. 3) for the five hits of *Wb*TPx1 are given in Table 2 where the glide score ranges from − 7.41 to − 6.88 kcal/mol and the glide energy lies from − 48.73 to − 36.22 kcal/mol. The 2D representation interaction map of the hits with the *Wb*TPx1, are shown in Fig. 4. The first hit, N-benzyl-N-(2-hydroxyethyl)-3-[5-(1H-indol-3-ylmethyl)-1,3,4-oxadiazol-2-yl] propenamide (ID-26319496) formed three hydrogen bonds with residues Ser168, Arg184 and Pro200 with the Glide score of − 7.41 kcal/mol.

The hit also formed three pi-pi stacking interactions with the His167 moiety. The second hit, 1-(3-{[(S*)-(cis-3-hydroxycyclo butyl) (phenyl)methyl]amino}-3-oxopropyl) piperidine-4-carboxamid (ID: 58522350) forms four hydrogen bonds with residues Ala28, Ser168, Arg184 and Trp203 with the Glide score of − 7.37 kcal/mol whereas the thirds hit, 4-[(1-{[3-(4-hydroxyphenyl)-1H-pyrazol-5-yl]carbonyl}pyrrolidin-3-yl)methyl]benzoic acid (ID: 24425757) exhibit three hydrogen bonds and a salt bridge with the residues Leu27, His167, Trp203 and Arg184 having the Glide score of − 7.13 kcal/mol.

The fourth hit, 1-{[5-(hydroxymethyl)-2-furyl] methyl}-N-[4-(1,3 -thiazol-4-yl)phenyl]-3-piperidine carboxamide (ID: 38651207) showed three hydrogen bonds and two pi-pi stacking with residues Leu27, Arg166, Ser168, His167, and Phe189 with the Glide score of − 6.93 kcal/ mol whereas the fifth hit, N-[(cis-3-hydroxycyclobutyl) (2-thienyl)methyl]-2-(2-oxoazepan-1-yl)acetamide (ID: 29025530) two hydrogen bonds and one pi-pi stacking with the residues Cys199, Trp203 and His167 having the Glide score of − 6.88 kcal/mol, respectively. The distance of H-bond occurred between the hit molecule and the protein is also one factor that decides the stability and strength of protein-hit complex formation. The H-bond is considered stronger if the distance is less than 2.5 Å, and it is considered moderate if it is between 2.5 and 3.5 Å [55, 62]. All five hits exhibited a strong H-bond with a distance lesser than 2.5 Å. Besides the bonded interactions, the stability and binding of potential hits are influenced by non-bonded

Table 1 Assessment of ADMET Properties in identified *Wb*Tpx1 Hits from ChemBridge small molecule collection

ADMET prediction of the top five potent hits of *Wb*Tpx1					
ChemBridge ID	26319496	58522350	24425757	38651207	29025530
Molecular weight[a]	404.468	359.467	391.426	397.491	336.448
QP logPo/w[b]	3.147	0.157	3.434	3.169	1.123
QP logS[c]	−4.944	−1.181	−5.635	−4.567	−2.091
QP logHERG[d]	−5.691	−3.493	−4.035	−7.402	−1.624
CIQPlogS[e]	−5.086	−0.841	−5.876	−3.961	−1.644
QPPCaco[f]	203.136	13.776	9.129	372.84	301.103
QPlogBB[g]	−1.824	−1.453	−2.326	−0.212	−0.826
QPlogKhsa[h]	0.004	−0.756	0.395	0.178	−0.700
PHOA[i]	86.678	48.25	64.239	91.524	77.882
QPlogKp[j]	−2.128	−5.674	−4.819	−3.448	−2.740
Rule of three[k]	0	1	1	0	0
Rule of five[l]	0	0	0	0	0
#stars[m]	0	0	0	0	0
Molecule toxicity prediction	Non toxic	Non toxic	Non toxic	Non toxic	Non toxic

[a]Hit molecular weight (130.0 to 725.0)

[b]Partition coefficient of octanol/water (−2.0 to 6.5)

[c]Aqueous solubility (−6.5 to 0.5)

[d]HERG K^+ channel blockage IC_{50} value (below −5)

[e]Conformation-independent predicted aqueous solubility (−6.5 to −0.5)

[f]Cell permeability of Caco-2. (>500 great; <25 poor)

[g]Partition coefficient for brain/blood. (−3.0 to 1.2)

[h]Human serum albumin binding. (−1.5 to −1.5)

[i]Human oral absorption (>80% is high; <25% is poor)

[j]Permeability in skin (−8.0 to −1.0)

[k]Jorgensen's rule of three. (0–3)

[l]Lipinski's rule of five (0–4)

[m]#stars drug likeness (0–5)
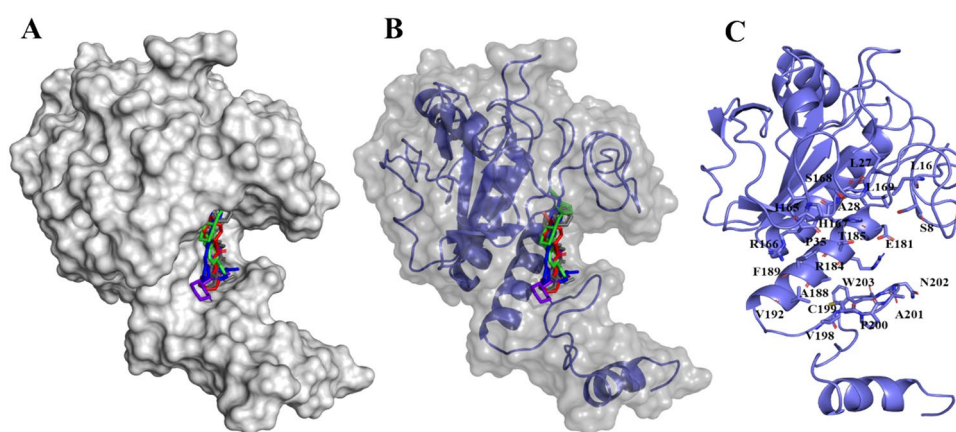
Fig. 3 **A** Structural alignment of top five hits which showed higher affinity with better satisfied the ADMET profile that bind in the binding site of *Wb*TPx1 were represented in black, red, blue, green, and purple (ID: 26319496, 58522350, 24425757, 38651207 & 29025530) sticks, respectively. **B** Surface representation rendered transparently and integrated with a blue cartoon shows the hits bound in the *Wb*TPx1 binding site. **C** Cartoon representation of the *Wb*TPx1 and the sticks represent the binding site residues that are labeled in single letter

Table 2 XP docking results along with binding free energies of the top five hits for *Wb*Tpx1

S. No	ChemBridge ID	Glide score (kcal/mol)	Glide energy (kcal/mol)	ΔG Bind (kcal/mol)	*Wb*Tpx1 Interaction	Bond Distance (Å)
1	26319496	− 7.410	− 48.739	− 47.15	Ser 168	1.90-HB acceptor
					Arg 184	2.00-HB donor
					Pro 200	1.80-HB acceptor
					His 167	pi–pi stacking
2	58522350	− 7.372	− 45.555	− 63.06	Ala 28	1.90-HB acceptor
					Ser 168	1.90-HB acceptor
					Arg 184	1.80-HB donor
					Trp 203	2.00-HB acceptor
3	24425757	− 7.134	− 43.417	− 50.15	Leu 27	1.90-HB acceptor
					His 167	2.10-HB acceptor
					Trp 203	2.40-HB donor
					Arg 184	1.9-SB
4	38,651,207	− 6.932	− 47.132	− 56.78	Leu 27	2.00-HB acceptor
					Arg 166	2.10-HB acceptor
					Ser 168	1.90-HB donor
					His 167	pi–pi stacking
					Phe 189	pi–pi stacking
5	29,025,530	− 6.887	− 36.292	− 48.81	Cys 199	2.00-HB donor
					Trp 203	2.60-HB acceptor
					His 167	pi–pi stacking

contributions, including charged, hydrophobic and polar groups of *Wb*TPx1. The Prime MMGBSA method uses the molecular mechanics and continuum solvation models to calculate the ΔG Bind (binding free energy) analysis between the docked complex structure of the selected five hit molecules of *Wb*TPx1. It showed the ΔG_{bind} values between − 47.15 and − 63.06 kcal/mol, which lies in the order of hit ID: 58522350 > 38651207 > 24425757 > 26319496 > 29025530. Further, the cross-docking study was performed with human TPx1 (PDB ID: 5UCX) to evaluate the drug specificity. Hs and *Wb*TPx1 show an identity of 56.19% with a structural RMSD value of 0.8 Å. Both organism exhibits similar thioredoxin structural folds, with five α-helices and seven β-strands which are the invariant features of members peroxiredoxins family. We have carried out cross-docking with the top five identified potent hits at the same dimer interface area of *Hs*TPx1 to confirm the selectivity of the identified hits towards the *Wb*TPx1. The extra Precision (XP) docking results showed the Glide score of − 3.14, − 3.33, − 4.51, − 1.75 and − 3.14 kcal/mol for the hits IDs: 26319496, 58522350, 24425757, 38651207, and 29025530, respectively. Additionally, we observed differences in the volume of the binding site cavity and the lack of bonded interaction between the hits and *Hs*Tpx1, which may account for the lower docking scores and affinity, and these results revealed that hits exhibit higher and strong affinity towards *Wb*. Thus, studies were carried out for these selected hit molecules to analyze binding stability and complex integrity.

Density functional theory (DFT) analysis of potent hits *Wb*TPx1

In quantum calculations, the HOMO and LUMO play a significant influence in reactivity of the hits. HOMO signifies an inclination to donate electrons, whereas the LUMO accepts electrons, and its energy aligns with the electron affinity. The energy gap (E_{gap}) is utilized to determine the chemical reactivity of the hits. The calculated energies of the LUMO orbital for five hits lie between − 0.02558 and − 0.06691 eV, whereas the HOMO orbital energies lies between − 0.20061 and − 0.24194 eV.

Additionally, the five hits energy gaps (E_{gap}) ranged from 0.12 to 0.29 eV (Table 3). The HOMO and LUMO energy of the five hits, along with the molecular orbitals diagram, are shown in Fig. 5. The distribution of energy in the hit molecules is shown by the colors green and red, which indicate the positive and negative charged moities. Based on E_{gap} value, the chemically reactive of the hits lies in the order of ChemBridge ID: (29025530 (0.20966 eV) > 58522350 (0.20094 eV) > 26,319,496 (0.18668 eV) > 38651207 (0.16548 eV) > 24425757 (0.15936 eV), respectively.

MD simulation: dynamic stability of hit-bound *Wb*Tpx1 complexes

MD simulations were carried out for all five hits bound to *Wb*Tpx1 individually to monitor the dynamicity of the complexes. All the five *Wb*Tpx1 complex systems (*Wb*Tpx1 + ChemBridge ID: 26319496, 58522350,
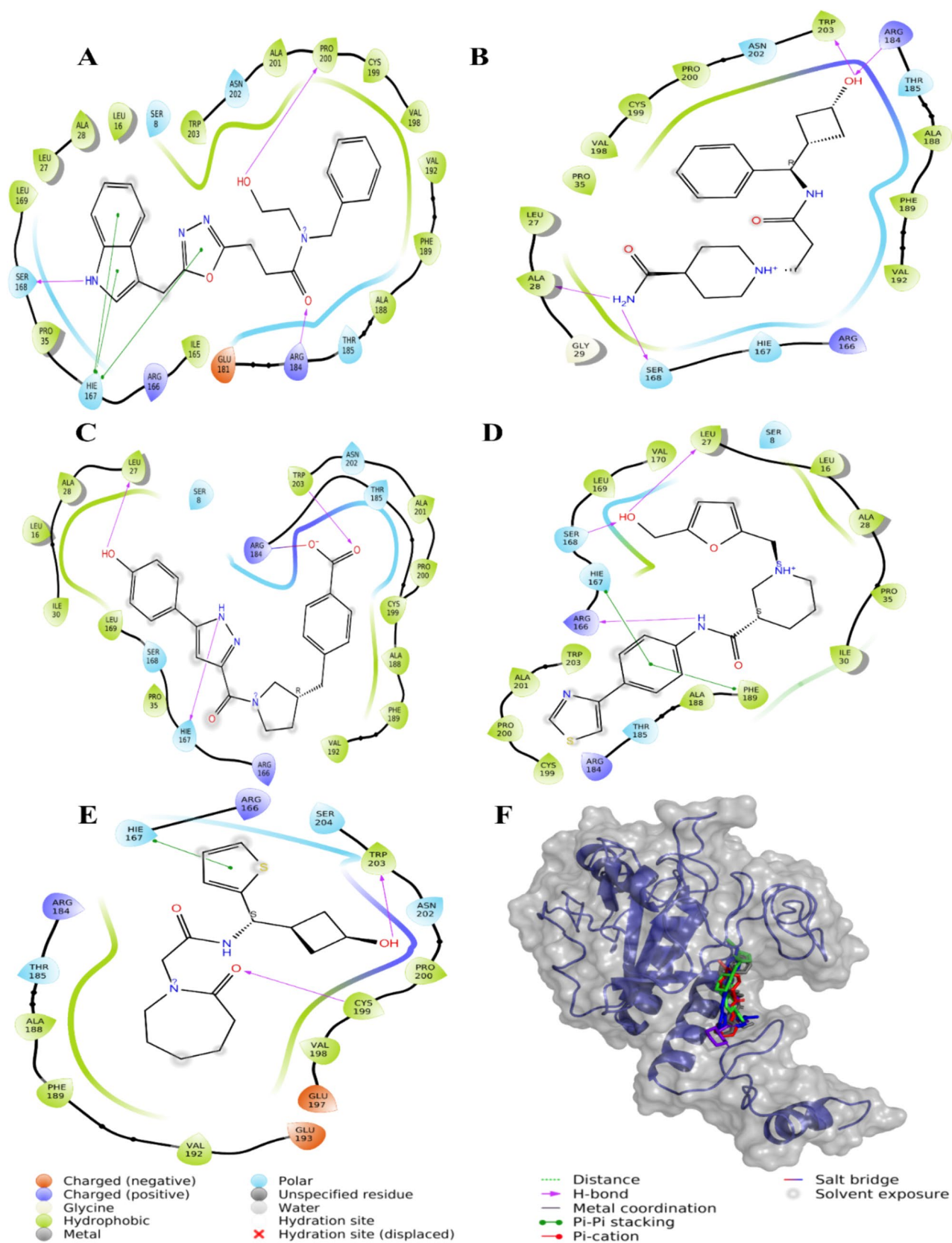
◄**Fig. 4** The 2D representation illustrating the ligand interaction map of the five hit molecules in the binding site of *Wb*TPx1 **A** 26319496, **B** 58522350, **C** 24425757, **D** 38651207 and **E** 38651207. The interaction profile indicates that hydrogen bonds and salt bridge interactions contribute to the stabilization of the hits with *Wb*TPx1. Additionally, the hits (26319496, 38651207 and 38651207) showed Pi–Pi interaction. **F** Surface representation rendered transparently and integrated with a blue cartoon shows the hits in the *Wb*TPx1 binding site

24425757, 38651207 & 29025530) attain equilibrium after 5 ns. The RMSD deviation of complex 1 (*Wb*Tpx1 + ChemBridge ID: 26319496) ranged from 0.30 to 0.44 nm, with average RMSD and SD value of 0.37 nm and 0.02 nm, whereas the complex 2 (*Wb*Tpx1 + ChemBridge ID: 58522350) and complex 3 (*Wb*Tpx1 + ChemBridge ID: 24425757) exhibited the RMSD deviation within 0.31 to 0.47 nm and 0.30 to 0.46 nm had the average of 0.38 and 0.39 nm and the standard deviation of 0.02 and 0.01 nm. Complex 4 (*Wb*Tpx1 + ChemBridge ID: 38,651,207) and 5 (*Wb*Tpx1 + ChemBridge ID: 29025530) showed similar trends in the RMSD values, that fluctuated between 0.33 and 0.52 nm and 0.41 to 0.55 nm showed the average of 0.42 and 0.45 nm with the standard deviation of 0.03 and 0.01 nm, respectively. To investigate the level fluctuations of residues upon hit binding, the backbone RMSF of *Wb*Tpx1 was examined. As observed in the native *Wb*Tpx1 all the five hit bound complexes exhibited higher reside-wise RMSF fluctuations in both the terminal regions due to the terminal flexibility. The N-terminal loop that spans from Met1 to Phe42 showed a higher RMSF value and similarly, the C-C-terminal from His195 to Thr228 has the highest RMSF value due to terminal flexibility. The loop-V spanning from the residues Thr116 to Pro129 and loop-VI from Glu143 to Arg154 was observed to exhibit higher RMSF value in all the five complex systems of *Wb*TPx1. The RMSF of the complex1 fluctuated between 0.05 and 0.69 nm with an average of 0.17 nm and the residue Ser119 of loop-V showed the highest backbone fluctuation of 0.29 nm whereas in loop-VI the residue His147 exhibit maximum fluctuation of 0.20 nm. In complexes 2 and 3, the average RMSF fluctuation was found to be 0.16 and 0.15 nm, exhibiting a similar range between 0.05 and 0.71 nm. In both complexes, the loop-V residue Ser119 displays higher fluctuations of 0.22 and 0.15 nm and the residue Glu148 of loop-VI shows larger backbone fluctuations of 0.17 and 0.21 nm, respectively. The average RMSF of complex 4 and 5 were found to be 0.16 and 0.17 nm with a range from 0.05 to 0.49 nm and 0.06 to 0.80 nm, respectively, where the loop-V residue Glu120 and Ser119 account for more fluctuation of 0.17 and 0.22 nm while the loop-VI the residue Glu148 was observed to have more fluctuation of 0.22 and 0.17 nm among other counterparts residues of loop-VI. The Rg

(radius of gyrations) measures the compactness of the hit-bound state of *Wb*TPx1, the five *Wb*Tpx1 complex systems exhibit intact Rg with the average value of 1.95, 1.93, 1.91, 1.93 and 1.92 nm with the SD of 0.02, 0.01, 0.01, 0.02 and 0.02, respectively. The SASA was also used to evaluate the complexes surface area that interacts with the nearby water molecules. The average SASA for *Wb*TPx1-hit complexes was determined to be 134.65, 135.07, 137.54, 131.70, and 132.69 nm^2, with corresponding standard deviations of 2.74, 3.17, 2.51, 3.16, and 2.78 nm^2, as seen in (Fig. 6).

The complex MD simulation based on the profiles of RMSF, RMSD, SASA and Rg revealed that throughout the simulation period, all the five hits (ChemBridge ID: 26319496, 58522350, 24425757, 38651207 & 29025530) bind intact inside the binding site of *Wb*TPx1. The simulated trajectories were analyzed by calculating Coulomb and L–J energies to examine non-bonded energy contributions in the interactions between *Wb*TPx1 and hit molecules. Table 4 signifies that the Lennard–Jones potential energy was more dominant than coulomb energy that accounts for the stability of the five complexes. Based on the calculation of binding energy, it is evident that non-bonded energies were also crucial in maintaining the intact and stable binding of hits within the *Wb*TPx1 throughout complex dynamics. Supplementary Fig. 3 showcases ensembles of *Wb*TPx1 complexes with hit molecules, captured every 10 ns throughout the simulation. Its evident from these snapshots that the hits remained securely bound within *Wb*TPx1 binding site throughout the entire simulation period.

Comparative PCA and FEL analysis of native and hit-bound dynamics

PCA projects the molecular trajectories generated in the MD simulation onto a 2D plane, with the first three principal components (PC1 to 3) elucidating the maximum variability in the data (Table 5). A comparison between the hits bound and native *Wb*TPx1 revealed that the native *Wb*TPx1 PC1 magnitude was smaller, whereas the magnitude of PC2 of the *Wb*TPx1 native is observed to be higher than the hits bound *Wb*TPx1. In the native system, the first two PCs account for 49.9% variability and the hit bound five systems (*Wb*Tpx1 + ChemBridge ID: 26319496, 58522350, 24425757, 38651207 & 29025530), the first two PCs contribute 49.61%, 50.02%, 48.47%, 51.93% and 60.85% as total variability of the systems. Therefore, the initial two eigenvectors, PC1 and PC2, encompassed the maximum principal variances in the original distribution of the conformational space within the simulation systems. This indicates that PC1 and PC2 predominantly reflect the shifts in the conformational state. PCA scatter plots comparing the native and hit-bound states of the *Wb*TPx1 simulation

Table 3 The chemical reactive qualities of the five potential hits of *Wb*Tpx1 obtained from DTF studies

S. No.	ChemBridge ID	HOMO (eV)	LUMO (eV)	Energy gap (eV)
1.	26319496	− 0.21789	− 0.03121	0.18668
2.	58522350	− 0.22652	− 0.02558	0.20094
3.	24425757	− 0.22629	− 0.06691	0.15936
4.	38651207	0.20061	− 0.03513	0.16548
5.	29025530	− 0.24194	− 0.03228	0.20966
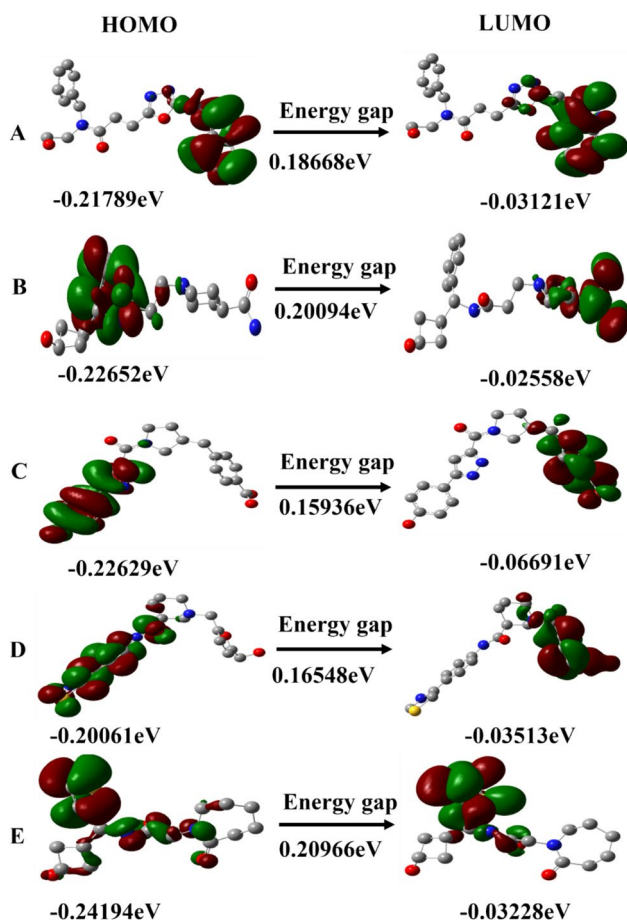
Fig. 5 HOMO and LUMO for the five potential hits **A** 26319496, **B** 58522350, **C** 24425757, **D** 38651207 and **E** 38651207 are shown with orbital contour map. The noticeable difference in energy gap between the LUMO and HOMO signifies the stability and chemical reactivity of the hits, revealing their strong binding affinity with *Wb*Tpx1

systems were generated by projecting along the directions of the first two principal components, PC1 and PC2, where the red and blue dots indicate the conformationally stable and unstable, respectively. The scatter plot distribution of native clearly showed irregular and messy. However, in the

case of five hits complex system the scatter plot was found to be well organized where the red and blue spots in clusters were equally spaced parallel to each other on both sides of the diagonal with respect to PC1, PC2 and PC3. This PCA clearly showed the intact and stable binding of the hits in the binding site of the *Wb*Tpx1 that remained consistent with the RMSD, RMSF, Rg and SASA analysis results.

Although the initial two principal components were adequate to explain the fluctuations in conformational changes and motion throughout the simulation, we also considered the variability explained by the PC3, which is clearly shown in supplementary Figs. 4, 5, 6, 7, 8, 9.

Further, the correlated motions at the residue level were also determined by analyzing the cross-correlation map of residues for the atoms in the backbone of both native *Wb*TPx1 and hit bound (*Wb*Tpx1 + ChemBridge ID: 26319496, 58522350, 24425757, 38651207 & 29025530). The maximum negative or anticorrelated backbone motion was represented by the magenta region that range from 0 to − 1, indicating that the residues shift in the opposite direction and the backbone motion with positive correlation of *Wb*TPx1 was showed by the cyan regions that range from 0 to 1, implying that the residues move in the same direction. The stronger the correlation, the darker the displayed color. The figure demonstrated that overall, the correlated motion of the two systems displayed a similar motion trend, but it was clear that these two systems correlated motion had altered upon binding of the hit molecules with the *Wb*Tpx1. Especially in key areas related to binding site regions (represented as black box in Fig. 7). It was generally believed that the reduction of negatively correlated motion would reduce the flexibility of the protein. Therefore, the five hits binding to the *Wb*Tpx1 binding site would hinder the complex systems correlated motion, making it more difficult for *Wb*Tpx1 to be exposed to forming dimers and thereby accomplishing the purpose of inhibiting protein activity. The cross-correlation map revealed that both native and hits bound *Wb*TPx1 exhibit a similar trend in the correlated motion among the backbone atoms of the residues. We observed a minute change in the motion of the residue's backbone located in N– C– terminals and in the dimer interface region where the hits bind with the *Wb*Tpx1, as shown in Fig. 7. The porcupine plotting was generated for the PC1 which accounts for the greatest variability of the native and hit-bound states to visualize the direction of movement of the backbone atoms. Observations indicated that the *Wb*TPx1 bound to hits exhibits reduced backbone atom movement compared to the native *Wb*TPx1 (Fig. 8) that in accordance with the results of PCA and cross-correlation analysis.

To explore the conformational dynamics of native and hits bound *Wb*TPx1 the FEL (free energy landscape) was
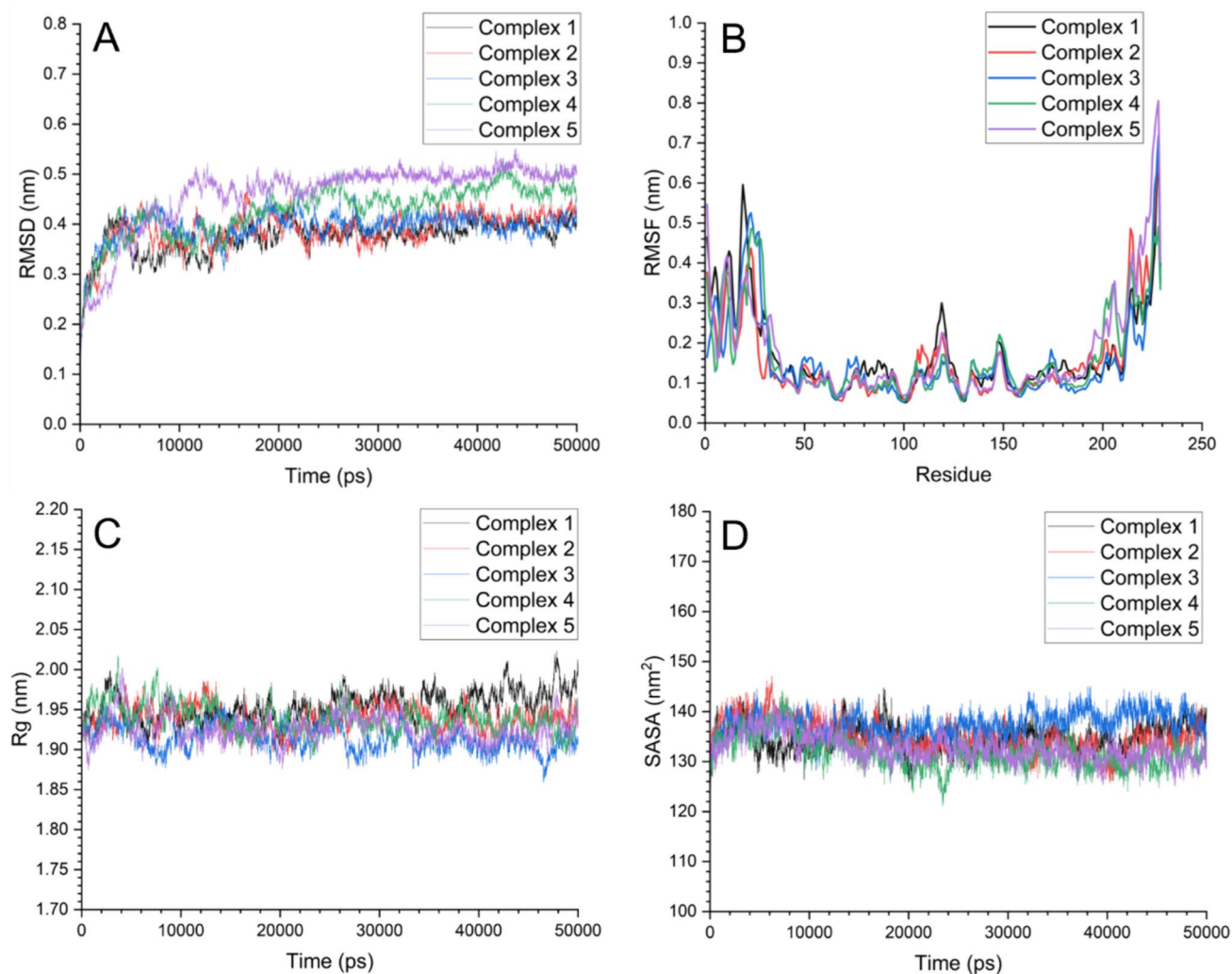
Fig. 6 The stability profiles: **A** RMSD, **B** RMSF, **C** Rg and **D** SASA are calculated from simulations for the *Wb*Tpx1—hits complexes: com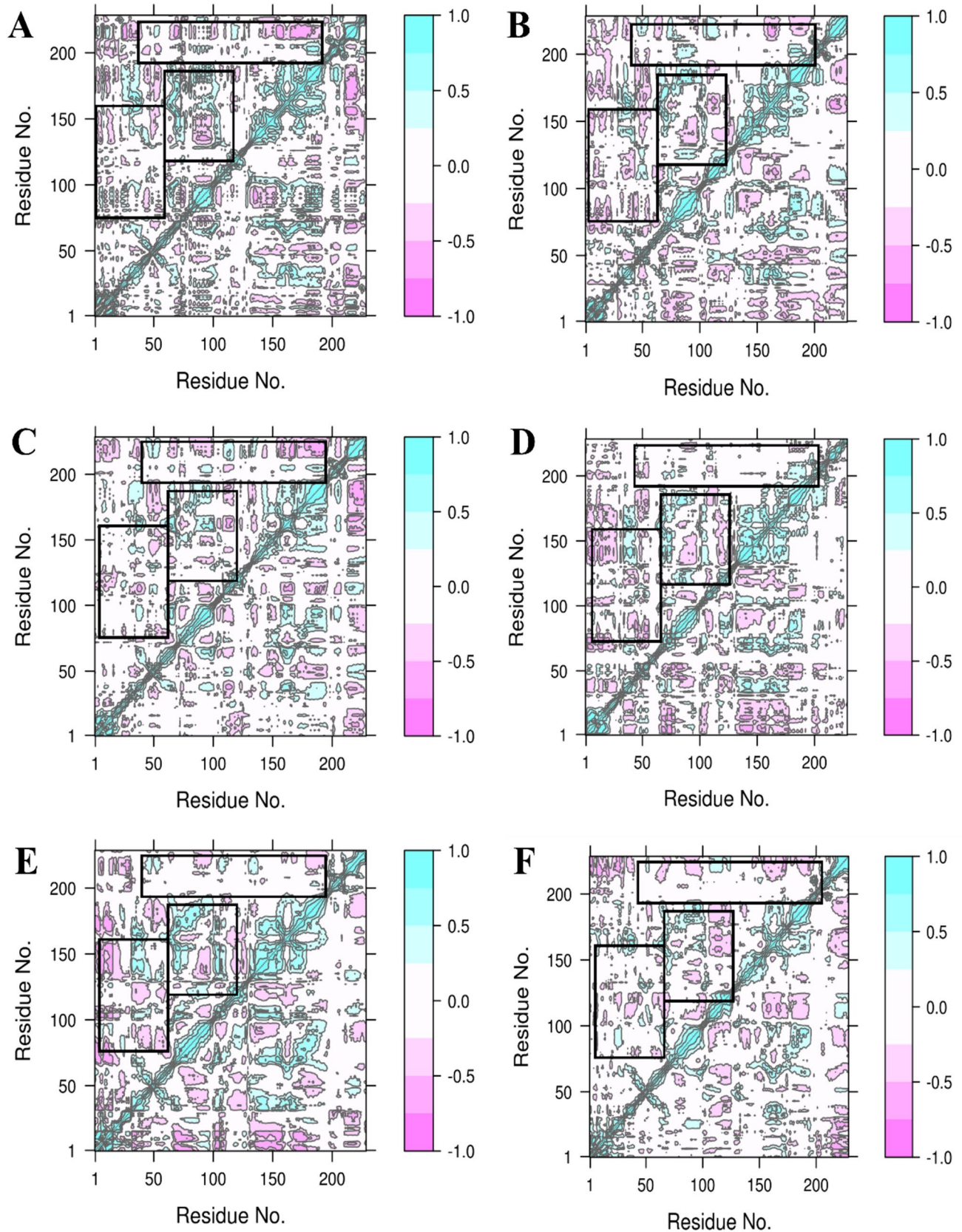plex 1–5 (26319496, 58522350, 24425757, 38651207 and 38651207) are showed in black, red, blue, green and purple, respectively, these analyses clearly indicate the intact and consistent bounding of the hits with *Wb*Tpx1 throughout complex simulations

Table 4 Coulomb and L–J energy contributions in interactions between *Wb*Tpx1 and non-toxic hits

Energy	ChemBridge ID				
	26319496	58522350	24425757	38651207	29025530
Coulomb energy (KJ/mol)	-62.30 ± 5.90	-44.22 ± 8.50	-58.93 ± 4.40	-37.65 ± 6.30	-38.31 ± 3.50
L–J Energy (KJ/mol)	-136.00 ± 4.10	-98.27 ± 8.10	-146.28 ± 3.0	-119.52 ± 7.30	-95.48 ± 4.70

Table 5 The initial three principle components from PCA of the hit-bound *Wb*Tpx1 and the native *Wb*Tpx1

Principal component	Native *Wb*Tpx1 (%)	ChemBridge ID				
		26319496 (%)	58522350 (%)	24425757 (%)	38651207 (%)	29025530 (%)
PC1	25.31	29.05	34.87	30.61	50.58	43.89
PC2	24.78	20.59	15.15	17.86	11.35	16.96
PC3	19.80	16.13	11.01	8.15	7.88	8.57

◄**Fig. 7** Cross-correlation map for **A** native *Wb*TPx1 and **B**–**F** hit bound *Wb*TPx1 (*Wb*TPx1- ChemBridge ID-26319496, 58522350, 24425757, 38651207 and 29025530 with positive correlation in cyan and negative (anticorrelation) in magenta colors, respectively. The black box highlighted the key areas where the correlated motions of the native and hit bound systems of *Wb*TPx1 were found to be significantly different

calculated. This enabled the observation of various states like local and global minima that are sampled throughout the entire time scale period of the MD simulation. The Gibbs free energy ranges from 0 to 11.50 kJ/mol for the native *Wb*TPx1 while for the complexes-*Wb*TPx1+ChemBridge ID: 26319496, 58522350, 24425757, 38651207 & 29025530, it ranges from 0 to 11.50,11.50,11.60, 13.40, and 11.60 kJ/mol and FEL is represented as contour diagram is shown in Fig. 9. The dark blue area indicates energetic minima and conformationally stable states, while the red and yellow sections show higher energy states.

The native *Wb*TPx1 exhibits a single global lowest energy conformation with a steep, narrow valley single basin. The FEL analysis of complexes 1 and 2 exhibit a similar trend in energy state with a broad basin that converges into numerous energy states from multiple local minimum states and confined to a single global energy state. The Complexes 3, 4, and 5 adopted a similar energy spread that of native, containing multiple local energy states but confined into a single sharp global minima energy state. Thus, FEL analysis offers atomic-level resolution of a protein–ligand bound system, identifies potential binding transition states and metastable states, and can be useful for designing inhibitors. The results of the essential dynamics, cross-correlation profile, porcupine and FEL analyses provide precise insights into the changes in the molecular conformational that occurred during MD simulation period as hits bound to the dimer interface site of *Wb*TPx1.

Viability evaluation of filarial worms through MTT-formazan colorimetric assay

The MTT assay was performed at concentrations spanning from 0.625 to 20 μM over a 24-h duration. At the maximum dosage of 20 mM concentration, three hits exhibited inhibition efficacy higher than 92% (94.50 ± 1.56, 93.83 ± 0.96 and 92.78 ± 0.91).

In contrast, at lower concentrations (0.625 μM), it showed the inhibition percentages of $32.70 \pm 0.74\%$, $38.79 \pm 0.85\%$ and $34.60 \pm 1.27\%$, respectively, for the hits- ChemBridge ID: 58522350, 24425757 and 26319496. Interestingly, all three hits had greater inhibition percentages at concentrations between 0.625 and 20 μM, that is found be to higher than the standard anti-filarial drug Ivermectin, as shown in Table 6. The IC_{50} values were calculated by the Michalis Menten equation and were matched with the standard drug ivermectin, IC_{50} value of hits of *Wb*TPx1 58522350, 24425757 and 26319496 lies between the range of 1.069 ± 0.204 μM, 1.373 ± 0.259 μM and 1.429 ± 0.246 μM. Interestingly, we noted that the IC_{50} value of two hits (24425757 & 26319496) was lesser than the IC_{50} value of Ivermectin with 1.374 ± 0.152 μM, shown in Fig. 10. The hits found using the in silico technique have the ability to eliminate adult worms, as revealed by the MTT reduction assay which showed better IC_{50} and higher inhibition than Ivermectin. Further, we employed molecular docking in the same binding site of *Wb*TPx1 to examine the interacting profile of Ivermectin. Interestingly, Ivermectin showed a glide score of -3.352 kcal/mol, suggesting a lower binding affinity than the identified potent hits of *Wb*TPx1, which ranged from -7.410 to -6.887 kcal/mol, the interaction profile of the Ivermectin with the *Wb*TPx1 is shown in Fig. 10. We observed two moderate hydrogen bonds with the distance of 2.9 Å and 3.0 Å between His 167 and Glu 181 of *Wb*TPx1 with Ivermectin. In the case of the identified five hit compounds, we observed the complex

Fig. 8 Porcupine plot illustrating the backbone atom movement for **A** native *Wb*TPx1 and **B–F** hit bound *Wb*TPx1 (*Wb*TPx1- ChemBridge ID-26319496, 58522350, 24425757, 38651207 and 29025530 from the trajectories. The directional arrows in the projection depict the movement of the *Wb*TPx1 backbone atoms
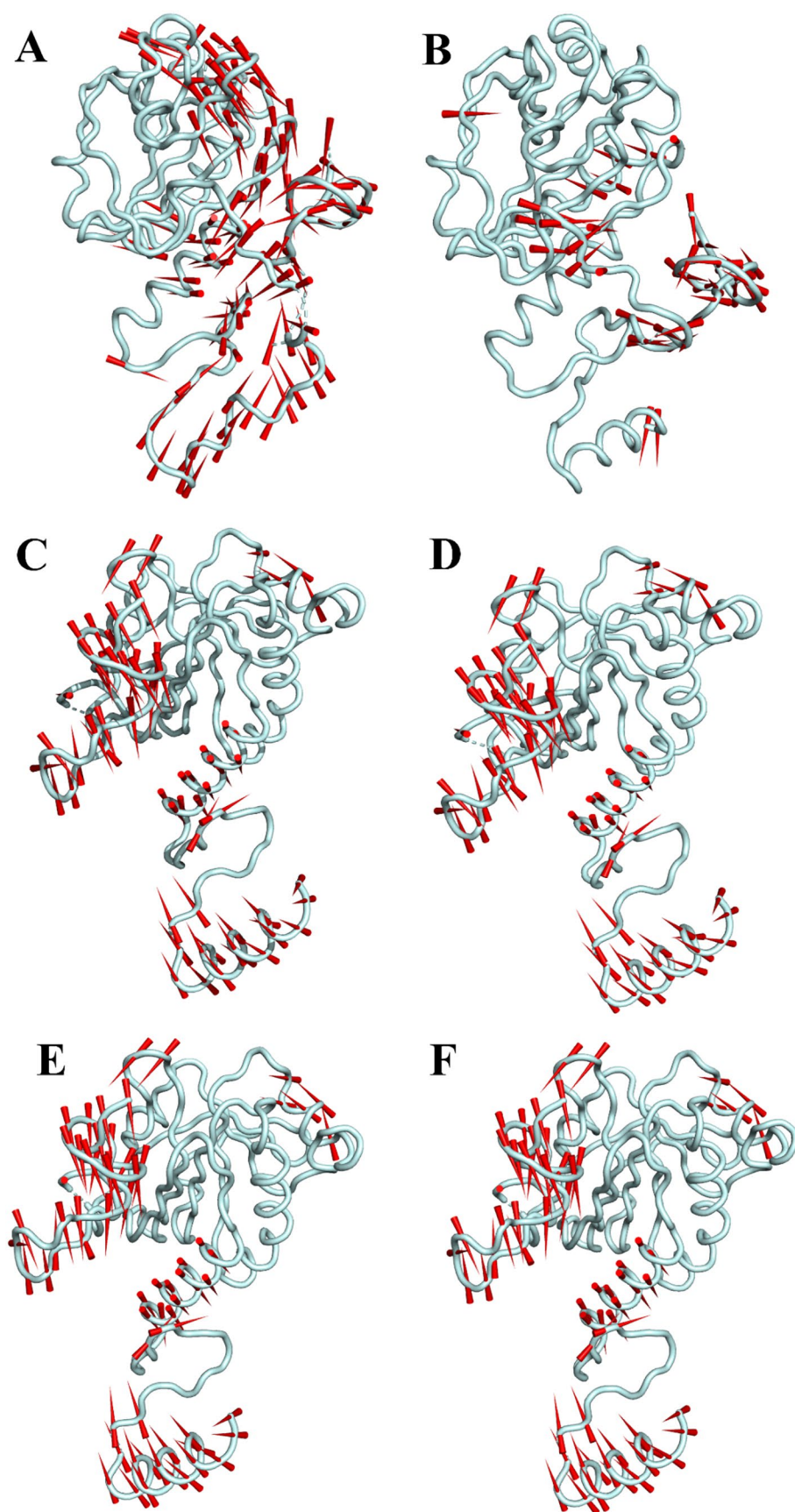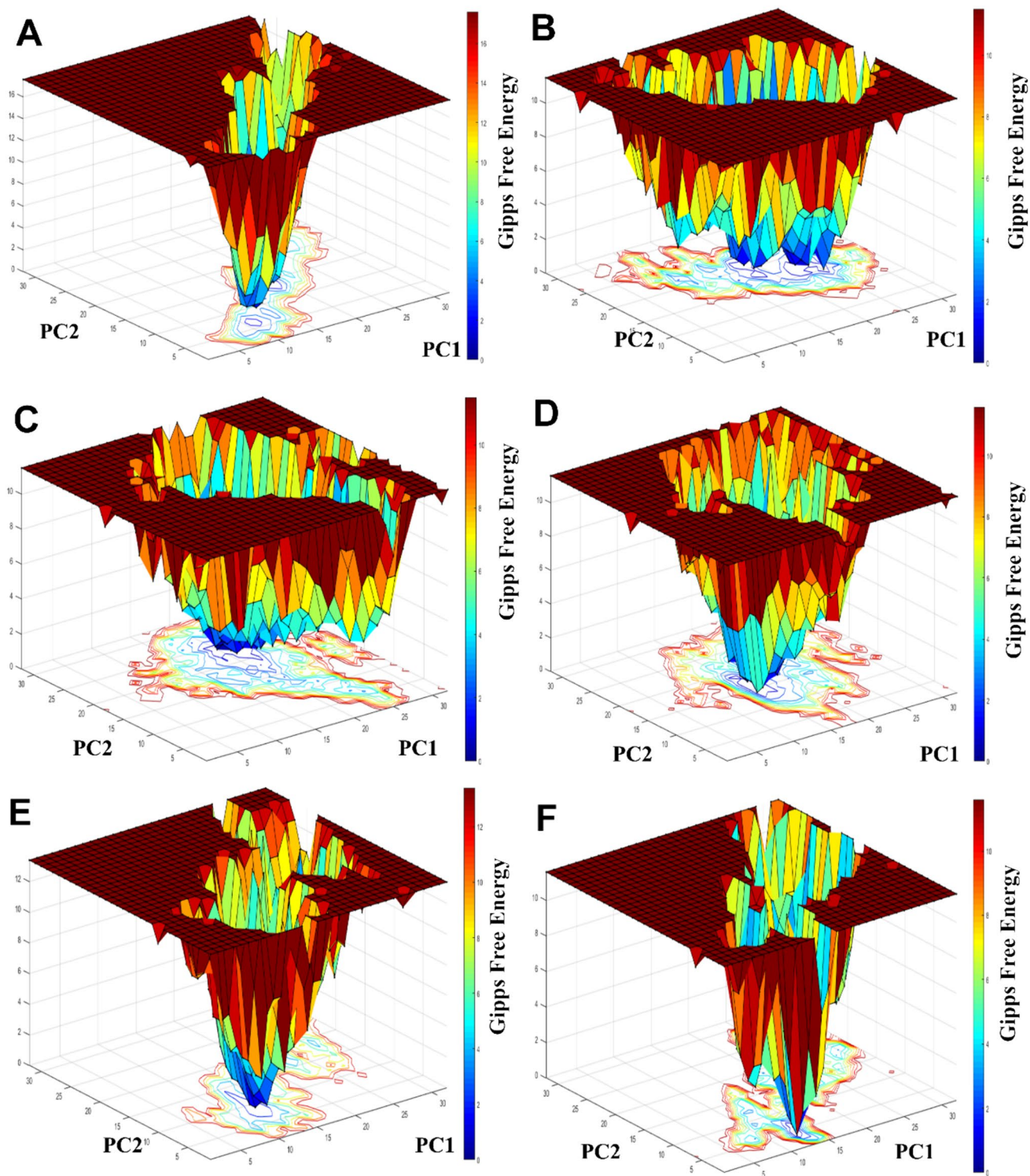
Fig. 9 The FEL comparison: **A** native *Wb*TPx1 and with five complexes **B–F** ((*Wb*TPx1- ChemBridge ID-26319496, 58522350, 24425757, 38651207 and 29025530)) The contour profile constructed based on first two principal components (PC1 & PC2) along the x, y axis and the z-axis represented by Gibbs free energy

Table 6 In vitro anti-filarial activity for hits of *Wb*Tpx1 and comparison of inhibition profile with Ivermectin using adult *S. digitata*

S. No	Concentration of inhibitor (µM)	Percentage of inhibition 58522350	Percentage of inhibition 24425757	Percentage of inhibition 26319496	Percentage of inhibition ivermectin
1	20.000	94.50 ± 1.56	93.83 ± 0.96	92.78 ± 0.91	83.08 ± 68
2	15.000	87.70 ± 0.95	83.72 ± 1.04	84.64 ± 0.74	77.82 ± 0.97
3	10.000	77.73 ± 2.10	75.37 ± 0.80	77.20 ± 1.19	71.94 ± 1.07
4	5.000	66.07 ± 2.29	70.75 ± 0.90	66.24 ± 0.74	62.52 ± 2.01
5	2.500	59.76 ± 1.44	60.75 ± 1.20	54.33 ± 0.85	53.25 ± 2.18
6	1.250	45.38 ± 1.26	47.32 ± 1.27	46.16 ± 1.46	42.96 ± 2.31
7	0.625	32.70 ± 0.74	38.79 ± 0.85	34.60 ± 1.27	27.40 ± 3.13

Fig. 10 **A** In vitro validation using the adult *S. digitata* worms, for top three hits of *Wb*Tpx1 along with the standard drug Ivermectin (ChemBridge ID-58522350, 24425757and 26319496) at different concentrations 0.625 to 20 µM, **B** two dimensional interaction profile of ivermectin interactions with the binding site residues of *Wb*Tpx1, where H-bonds were represented by solid arrows and **C** transparent surface representation embedded with blue cartoon representation clearly showing the ivermectin bind in the binding site of *Wb*Tpx1
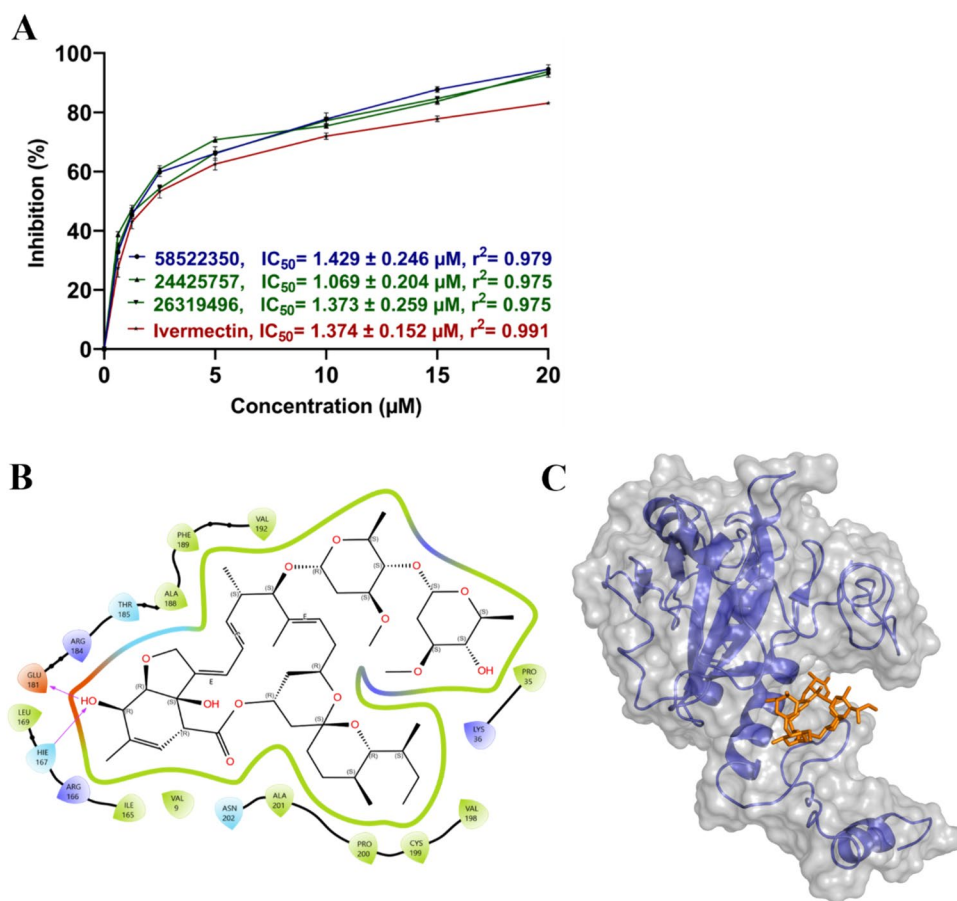
is stabilized by the hydrogen bonds, salt bridge, Pi–Pi interaction and hydrophobic interactions that accounts for higher binding affinity and these interaction profiles were found to be less prevalent in Ivermectin- *Wb*TPx1 complex.

Conclusion

Our current research is primarily on employing structure-guided drug design to identify potent inhibitors targeting the dimer interface region of *Wb*TPx1. The *Wb*TPx1 exhibited higher binding affinity with the five best non-toxic hits obtained from ChemBridge database (ChemBridge

ID-26319496, 58522350, 24425757, 38651207 & 29025530). The reactive of the hits were found using the DFT analysis, which also revealed important information for further hit enrichment and enhanced activity. Furthermore, the MD simulation studies of these *Wb*TPx1-hit complexes demonstrated that all five hits were found to be intact and bound inside the *Wb*TPx1 binding region. Its interesting to note that these five hits showed more binding selectivity for *Wb* than for *Hs*. The in vitro validation suggested that, in comparison to the standard medicine Ivermectin, the two discovered hits (ID: 24425757 & 26319496) showed a better percentage of inhibition and an improved IC_{50}. In future these identified hit molecules are the starting point for improvement of innovative small molecular chemical scaffolds and fragments that can be enriched using in vitro and in vivo models that likely could delivered strong drug-like characteristics features which might helpful towards addressing LF infections.

Declarations

Competing interests The authors declare no competing interests.

References

1. Simonsen PE, Mwakitalu ME (2013) Urban lymphatic filariasis. Parasitol Res 112:35–44. https://doi.org/10.1007/s00436-012-3226-x

2. Routh HB, Bhowmik KR (1993) History of elephantiasis. Int J Dermatol 32:913–916. https://doi.org/10.1111/j.1365-4362.1993.tb01418.x

3. Michael E, Bundy DAP, Grenfell BT (1996) Re-assessing the global prevalence and distribution of lymphatic filariasis. Parasitology 112:409–428. https://doi.org/10.1017/s0031182000066646

4. Ramaiah KD, Das PK, Michael E, Guyatt HL (2000) The economic burden of lymphatic filariasis in India. Parasitol Today 16:251–253. https://doi.org/10.1016/s0169-4758(00)01643-4

5. Bizhani N, Hashemi Hafshejani S, Mohammadi N et al (2021) Lymphatic filariasis in Asia: a systematic review and meta-analysis. Parasitol Res 120:411–422. https://doi.org/10.1007/s00436-020-06991-y

6. Famakinde DO (2018) Mosquitoes and the lymphatic filarial parasites: research trends and budding roadmaps to future disease eradication. Trop Med Infect Dis 3:4. https://doi.org/10.3390/tropicalmed3010004

7. Freedman DO (1998) Immune dynamics in the pathogenesis of human lymphatic filariasis. Parasitol Today 14:229–234. https://doi.org/10.1016/S0169-4758(98)01244-7

8. Paily KP, Hoti SL, Das PK (2009) A review of the complexity of biology of lymphatic filarial parasites. J Parasit Dis 33:3–12. https://doi.org/10.1007/s12639-009-0005-4

9. Rao UR, Chandrashekar R, Subrahmanyam D (1987) Effect of ivermectin on serum dependent cellular interactions to Dipetalonema viteae microfilariae. Trop Med Parasitol 38:123–127

10. Critchley J, Addiss D, Gamble C et al (2005) Albendazole for lymphatic filariasis. Cochrane Database Syst Rev. https://doi.org/10.1002/14651858.cd003753.pub3

11. Reaves BJ, Wallis C, McCoy CJ et al (2018) Recognition and killing of *Brugia malayi* microfilariae by human immune cells is dependent on the parasite sample and is not altered by ivermectin treatment. Int J Parasitol Drugs drug Resist 8:587–595. https://doi.org/10.1016/j.ijpddr.2018.09.002

12. Kwarteng A, Ahuno ST, Akoto FO (2016) Killing filarial nematode parasites: role of treatment options and host immune response. Infect Dis poverty 5:86. https://doi.org/10.1186/s40249-016-0183-0

13. Cobo F (2016) Determinants of parasite drug resistance in human lymphatic filariasis. Rev Esp Quimioter 29:288–295

14. Weiss SJ, Test ST, Eckmann CM et al (1986) Brominating oxidants generated by human eosinophils. Science 234:200–203. https://doi.org/10.1126/science.3018933

15. Cross AR, Jones OTG (1991) Enzymic mechanisms of superoxide production. BBA: Bioenerg 1057:281–298. https://doi.org/10.1016/s0005-2728(05)80140-9

16. Callahan HL, Crouch RK, James ER (1988) Helminth anti-oxidant enzymes: a protective mechanism against host oxidants? Parasitol Today 4:218–225. https://doi.org/10.1016/0169-4758(88)90162-7

17. Selkirk ME, Smith VP, Thomas GR, Gounaris K (1998) Resistance of filarial nematode parasites to oxidative stress. Int J Parasitol 28:1315–1332. https://doi.org/10.1016/s0020-7519(98)00107-6

18. Gretes MC, Poole LB, Karplus PA (2012) Peroxiredoxins in parasites. Antioxid Redox Signal 17:608–633. https://doi.org/10.1089/ars.2011.4404

19. Wood ZA, Schröder E, Robin Harris J, Poole LB (2003) Structure, mechanism and regulation of peroxiredoxins. Trends Biochem Sci 28:32–40. https://doi.org/10.1016/s0968-0004(02)00003-8

20. Flohé L (2010) Changing paradigms in thiology from antioxidant defense toward redox regulation. Methods Enzymol 473:1–39. https://doi.org/10.1016/s0076-6879(10)73001-9

21. Knoops B, Loumaye E, Van Der Eecken V (2007) Evolution of the peroxiredoxins. Subcell Biochem 44:27–40. https://doi.org/10.1007/978-1-4020-6051-9_2

22. Hakimi H, Asada M, Angeles JMM et al (2012) Cloning and characterization of *Plasmodium* vivax thioredoxin peroxidase-1. Parasitol Res 111:525–529. https://doi.org/10.1007/s00436-012-2864-3

23. Dayer R, Fischer BB, Eggen RIL, Lemaire SD (2008) The peroxiredoxin and glutathione peroxidase families in *Chlamydomonas reinhardtii*. Genetics 179:41–57. https://doi.org/10.1534/genetics.107.086041

24. Selkirk ME, Smith VP, Thomas GR et al (1998) Resistance of filarial nematode parasites to oxidative stress. Int J Parasitol 28:1315–1332. https://doi.org/10.1016/s0020-7519(98)00107-6

25. Prime (2020) Schrödinger Release 2020–4. Schrödinger, LLC, New York

26. Abraham MJ, Murtola T, Schulz R et al (2015) GROMACS: High performance molecular simulations through multi-level parallelism from laptops to supercomputers. SoftwareX 1–2:19–25. https://doi.org/10.1016/j.softx.2015.06.001

27. Oostenbrink C, Villa A, Mark AE, Van GWF (2004) A biomolecular force field based on the free enthalpy of hydration and solvation: the GROMOS force-field parameter sets 53A5 and 53A6. J Comput Chem 25:1656–1676. https://doi.org/10.1002/jcc.20090

28. Berendsen HJC, Postma JPM, van Gunsteren WF, Hermans J (1981) Interaction models for water in relation to protein hydration. In: Pullman B (ed) Intermolecular forces. Springer, Dordrecht, pp 331–342. https://doi.org/10.1007/978-94-015-7658-1_21

29. Vrahatis MN, Androulakis GS, Lambrinos JN, Magoulas GD (2000) A class of gradient unconstrained minimization algorithms with adaptive stepsize. J Comput Appl Math 114:367–386. https://doi.org/10.1016/s0377-0427(99)00276-9

30. Berendsen HJCC, Postma JPMM, Van Gunsteren WF et al (1984) Molecular dynamics with coupling to an external bath. J Chem Phys 81:3684–3690. https://doi.org/10.1063/1.448118

31. Parrinello M, Rahman A (1981) Polymorphic transitions in single crystals: a new molecular dynamics method. J Appl Phys 52:7182–7190. https://doi.org/10.1063/1.328693

32. Hess B (2008) P-LINCS: a parallel linear constraint solver for molecular simulation. J Chem Theory Comput 4:116–122. https://doi.org/10.1021/ct700200b

33. Miyamoto S, Kollman PA (1992) Settle: An analytical version of the SHAKE and RATTLE algorithm for rigid water models. J Comput Chem 13:952–962. https://doi.org/10.1002/jcc.540130805

34. Darden T, York D, Pedersen L (1998) Particle mesh Ewald: An N·log(N) method for Ewald sums in large systems. J Chem Phys 98:10089–10092. https://doi.org/10.1063/1.464397

35. Humphrey W, Dalke A, Schulten K (1996) VMD: visual molecular dynamics. J Mol Graph 14:33–38. https://doi.org/10.1016/0263-7855(96)00018-5

36. LigPrep (2020) Schrödinger Release 2020-4. Schrödinger, LLC, New York

37. Harder E, Damm W, Maple J et al (2015) OPLS3: a force field providing broad coverage of drug-like small molecules and proteins. J Chem Theory Comput 12:281–296. https://doi.org/10.1021/acs.jctc.5b00864

38. Schrödinger Release 2020-4 (2020) SiteMap. Schrödinger, LLC, New York

39. Friesner RA, Banks JL, Murphy RB et al (2004) Glide: a new approach for rapid, accurate docking and scoring. 1. Method and assessment of docking accuracy. J Med Chem 47:1739–1749. https://doi.org/10.1021/jm0306430

40. Frisch MJ, Trucks GW, Schlegel HB, et al (2016) G16_D09. Gaussian 16, Revision D.09, Gaussian, Inc., Wallin

41. Zhan C-G, Nichols JA, Dixon DA et al (2003) Ionization potential, electron affinity, electronegativity, hardness, and electron excitation energy: molecular properties from density functional theory orbital energies. J Phys Chem A 107:4184–4195. https://doi.org/10.1021/jp0225774

42. Schüttelkopf AW, van Aalten DMF (2004) PRODRG: a tool for high-throughput crystallography of protein-ligand complexes. Acta Crystallogr D Biol Crystallogr 60:1355–1363. https://doi.org/10.1107/s0907444904011679

43. David CC, Jacobs DJ (2014) Principal component analysis: a method for determining the essential dynamics of proteins. Methods Mol Biol 1084:193–226. https://doi.org/10.1007/978-1-62703-658-0_11

44. Hayward S, de Groot BL (2008) Normal modes and essential dynamics. Methods Mol Biol 443:89–106. https://doi.org/10.1007/978-1-59745-177-2_5

45. Wolf A, Kirschner KN (2013) Principal component and clustering analysis on molecular dynamics data of the ribosomal L11·23S subdomain. J Mol Model 19:539–549. https://doi.org/10.1007/s00894-012-1563-4

46. Maddah M, Karami L (2021) An atomistic investigation on the interaction of distamycin A and its derivative with the telomeric G-Quadruplex as anticancer agents by molecular dynamics simulation. Arch Biochem Biophys 701:108797. https://doi.org/10.1016/J.ABB.2021.108797

47. Grant BJ, Rodrigues APC, ElSawy KM et al (2006) Bio3d: an R package for the comparative analysis of protein structures. Bioinformatics 22:2695–2696. https://doi.org/10.1093/bioinformatics/btl461

48. Senanayake KS, Söderberg J, Põlajev A et al (2020) The genome of *Setaria digitata*: a cattle nematode closely related to human filarial parasites. Genome Biol Evol 12:3971–3976. https://doi.org/10.1093/gbe/evaa017

49. Perumal ANI, Gunawardene YINS, Dassanayake RS (2016) *Setaria digitata* in advancing our knowledge of human lymphatic filariasis. J Helminthol 90:129–138. https://doi.org/10.1017/s0022149x15000309

50. Mathew N, Karunan T, Srinivasan L, Muthuswamy K (2010) Synthesis and screening of substituted 1,4-naphthoquinones (NPQs) as antifilarial agents. Drug Dev Res 71:188–196. https://doi.org/10.1002/ddr.20357

51. Nisha M, Kalyanasundaram M, Paily KP et al (2006) In vitro screening of medicinal plant extracts for macrofilaricidal activity. Parasitol Res 100:575–579. https://doi.org/10.1007/s00436-006-0294-9

52. Senathilake KS, Karunanayake EH, Samarakoon SR et al (2017) Oleanolic acid from antifilarial triterpene saponins of *Dipterocarpus zeylanicus* induces oxidative stress and apoptosis in filarial parasite *Setaria digitata* in vitro. Exp Parasitol 177:13–21. https://doi.org/10.1016/j.exppara.2017.03.007

53. Mathew N, Misra-Bhattacharya S, Perumal V, Muthuswamy K (2008) Antifilarial lead molecules isolated from *Trachyspermum ammi*. Molecules 13:2156–2168. https://doi.org/10.3390/molecules13092156

54. Sureshan M, Prabhu D, Rajamanikandan S, Saraboji K (2023) Discovery of potent inhibitors targeting Glutathione S-transferase of *Wuchereria bancrofti*: a step toward the development of effective anti-filariasis drugs. Mol Divers 1:1–21. https://doi.org/10.1007/s11030-023-10617-7

55. Sureshan M, Prabhu D, Kadhirvel S (2023) Computational identification and experimental validation of anti-filarial lead molecules targeting metal binding/substrate channel residues of

Cu/Zn SOD1 from *Wuchereria bancrofti*. J Biomol Struct Dyn 41:1–14. https://doi.org/10.1080/07391102.2022.2136245

56. Choi J, Choi S, Choi J et al (2003) Crystal structure of *Escherichia coli* thiol peroxidase in the oxidized state: insights into intramolecular disulfide formation and substrate binding in atypical 2-Cys peroxiredoxins. J Biol Chem 278:49478–49486. https://doi.org/10.1074/jbc.m309015200

57. Nguyen JB, Pool CD, Wong CYB et al (2013) Peroxiredoxin-1 from the human hookworm *Ancylostoma ceylanicum* forms a stable oxidized decamer and is covalently inhibited by conoidin A. Chem Biol 20:991–1001. https://doi.org/10.1016/j.chembiol.2013.06.011

58. Goyal B, Goyal D (2020) Targeting the dimerization of the main protease of coronaviruses: a potential broad-spectrum therapeutic strategy. ACS Comb Sci 22:297–305. https://doi.org/10.1021/acscombsci.0c00058

59. Gunderwala AY, Nimbvikar AA, Cope NJ et al (2019) Development of allosteric BRAF peptide inhibitors targeting the dimer interface of BRAF. ACS Chem Biol 14:1471–1480. https://doi.org/10.1021/acschembio.9b00191

60. Cardinale D, Guaitoli G, Tondi D et al (2011) Protein-protein interface-binding peptides inhibit the cancer therapy target human thymidylate synthase. Proc Natl Acad Sci U S A 108:E542-549. https://doi.org/10.1073/pnas.1104829108

61. Kiss R, Sandor M, Szalai FA (2012) http://Mcule.com: a public web service for drug discovery. J Cheminform 4:P17. https://doi.org/10.1186/1758-2946-4-S1-P17

62. Sindhu T, Venkatesan T, Prabhu D et al (2018) Insecticide-resistance mechanism of *Plutella xylostella* (L.) associated with amino acid substitutions in acetylcholinesterase-1: a molecular docking and molecular dynamics investigation. Comput Biol Chem 77:240–250. https://doi.org/10.1016/j.compbiolchem.2018.09.004